Enabling Tunable Water-Responsive Surface Adaptation of PDMS via Metal-ligand Coordinated Dynamic Networks

*Xinyue Zhang Ralph Crisci John A. Finlay Hongyi Cai Anthony S. Clare Zhan Chen Meredith N. Silberstein**

Xinyue Zhang, Hongyi Cai
Department of Materials Science and Engineering, Cornell University, Ithaca, NY 14850, USA
Ralph Crisci, Prof. Zhan Chen
Department of Chemistry, University of Michigan, Ann Arbor, MI 48109, USA
Dr. John A. Finlay, Prof. Anthony S. Clare
School of Natural and Environmental Sciences, Newcastle University, Newcastle Upon Tyne, NE1 7RU, UK
Prof. Meredith N. Silberstein
Sibley School of Mechanical and Aerospace Engineering, Cornell University, Ithaca, NY 14853, USA
Email Address: meredith.silberstein@cornell.edu

Keywords: *dynamic network; metal-ligand coordination; stimulus response; surface adaptation; PDMS*

Polymers are at the core of emerging flexible sensor and soft actuator technology. Ideal candidates not only respond to external stimuli but also have programmable response intensity and speed. Incorporating dynamic interactions into polymers has been widely studied. However, most research has focused on synthesis methods and on optical and mechanical effects of these interactions. Here, we introduce a new and tunable method of enabling environmentally adaptive polymers. Specifically, we "hide" polar functionalities within PDMS. When unveiled, these polar functionalities change the hydrophilicity of the polymer. Water is the stimulus that triggers the exposure of polar functionalities by disrupting interfacial equilibrium and driving surface reconstruction. This reversible adaptation is governed by the dynamics of a metal-ligand coordinated polymer, and therefore can be easily tailored by the choice of network structure, metal cations, and counter anions. PDMS is a particularly exciting polymer for this functionality because of the negative consequences of its intrinsically high hydrophobicity in many applications. However, this design concept is applicable to a wide range of polymers and can be expanded to other dynamic interactions such as reversible covalent bonding, hydrogen bonding, and ionic bonding, to empower programmable responsive functionality and therefore enhance material performance.

1 Introduction

Flexible sensors and soft actuators which exhibit mechanical compliance, environment adaptation and stimuli response are emerging as an enabling technology.[1, 2, 3, 4] The combination of flexibility and responsiveness allows applications in various fields, including wearable electronics, soft robotics, drug delivery, biomedical devices and biomimetic design.[5, 6, 7, 8, 9, 10] Among various material options, polymers play an essential role in fabricating flexible sensors and soft actuators due to their tailorability and the potential of integrating multiple functionalities, such as adaptive response to signals (e.g. chemical, mechanical, electrical), energy harvesting and storage, and biochemical sensing.[3, 10] Adding responsive functionality to a polymer often involves methods such as copolymerizing monomers with different capability, attaching layers of active materials to a polymer matrix, building in molecular orientation or internal polarization, introducing structural heterogeneity by combining amorphous and crystalline domain or multi-layer assembly, and preparing composites by hybridizing organic and inorganic materials.[2, 11, 12, 13, 14]

Among various techniques, utilizing dynamic chemistry to enable polymer responsivity has received significant attention in the past few decades.[15, 16] Reversible interactions, including dynamic covalent bonding, hydrogen bonding, ionic bonding, π-π stacking, and metal–ligand coordination, are susceptible to environmental variation and can achieve multiple physical and chemical responses via bond breaking and reforming. [17, 18, 19, 20, 21] Fascinating material properties arise from disrupting the equilibrium state of dynamic bonding, for example: polymers with spiropyran go through force-induced covalent-bond activation and give rise to visible colour and fluorescence; supramolecular polymers containing metal–ligan motifs can self-heal by exposing to ultraviolet irradiation; and polymers functionalized by self-complementary hydrogen bonded ureidopyrimidinone (UPy) moieties shows shape-memory effect through temperature

This is the author manuscript accepted for publication and has undergone full peer review but has not been through the copyediting, typesetting, pagination and proofreading process, which may lead to differences between this version and the Version of Record. Please cite this article as doi: 10.1002/admi.202200430

change.[22, 23, 24] Among these options, metal-ligand coordination bonding is particularly appealing to realize a particular desired response, because of the ease of tuning the stability of the bond.

One of the most popular polymers for fabricating sensors and actuators is polydimethylsiloxane (PDMS).[2, 7] It commonly serves as an essential substrate or a responsive component due to the attractive physical and chemical properties, including low cost, flexibility, chemical inertness, biocompatibility, and ease of fabrication.[25, 26, 7, 27, 28] A primary shortcoming of PDMS, which often raise difficulties for functionalization and shortens the product lifetime, is the surface properties. First, the low surface energy of PDMS ($\sim$ 20 mN/m) yields weak interactions with other materials at the interface; second, the presence of methyl side groups causes inherently high hydrophobicity (contact angle $\sim$ 110 $\pm$ 10 °), making it challenging to wet by aqueous solutions and favoring undesired adsorption of substances at the PDMS-water interface.[29, 28] Therefore, surface treatments and bulk modifications have been developed to produce a hydrophilic PDMS surface, for example: applying oxygen plasma or UV radiation; coating a hydrophilic layer made of polyethylene glycol (PEG) or zwitterionic polymers; incorporating a hydrophilic block within a copolymer.[28, 30, 31] In the meantime, many efforts have been made to functionalize PDMS with stimuli-responsibility, for example: a PDMS with reversible wettability triggered by temperature change was made by UV-induced surface grafting of poly(N-Isopropylacrylamide) (PNIPAAm); a tough yet self-healable elastomer was synthesized by linking PDMS oligomers with urea units; and an electrically conductive film was fabricated by patterning liquid-metal circuits on a PDMS substrate. [32, 33, 34] However, these polymer modification methods involve complicated and expensive synthesis and/or processing.

In this paper, we present a simple and efficient method of functionalizing polymers with "hidden" polar functionality to enable water-responsive surface adaptation. Specifically, by embedding metal-ligand coordination into PDMS, a hydrophobic to hydrophilic evolution with tunable extent and speed is realized when the surface is exposed to water, and a hydrophobic restoration happens when water is removed. Metal-ligand coordination provides polar functionality and imparts a dynamic nature into the polymer network, leading to a reversible hydrophobic-hydrophilic transition that is controlled by the network architecture and coordination bond stability[21] Moreover, metal-ligand coordination offers the ease and versatility of switching design parameters, such as ligand species, network topology, metal cations, and counter anions, which facilitates programming the hydrophilicity of the materials for various purposes.[35, 21, 36] We first demonstrate the feasibility of the design by comparing the ligand functionalized PDMS with different network architectures but the same metal salt type and density of coordination bonds, and then tune the coordination strength of the model system by switching counter anions and metal cations. The network dynamics were characterized by mechanical tests, and the hydrophilicity of the coordinated PDMS was monitored by water contact angle. Sum Frequency Generation (SFG) vibrational spectroscopy, a second-order nonlinear optical spectroscopy technique,[37, 38, 39, 40, 41] was applied to probe surface chemical structures of PDMS materials in air and in water as well as time-dependent interfacial structural changes. The water wetting mechanism is discussed in the context of network dynamics. Finally, as one example of how such a surface adaptive polymer could enhance functionality, we demonstrate improved performance of the polymer against diatom biofouling. The insights included in this paper introduce fundamental design ideas for adapting polymer functionality, which is applicable to enhancing a wide range of polymers.

2 Results and Discussion

2.1 Metal-Ligand Coordination in PDMS to Control Surface Hydrophilicity

Metal-ligand coordination offers great flexibility in terms of designing the physical and chemical characteristics of a polymer network. To prove the idea that the progression of hydrophilicity enabled by exposing a "hidden" polar functionality in metal-ligand coordinated PDMS can be tuned by controlling the network dynamics, we carefully selected the structure of the model system: the PDMS backbone is free from entanglement to ensure chain mobility, and both chain ends are capped by pyridyl imine bidentate ligands to be able to coordinate with various metal salts.[42, 43, 44] Experimentally, the pyridyl

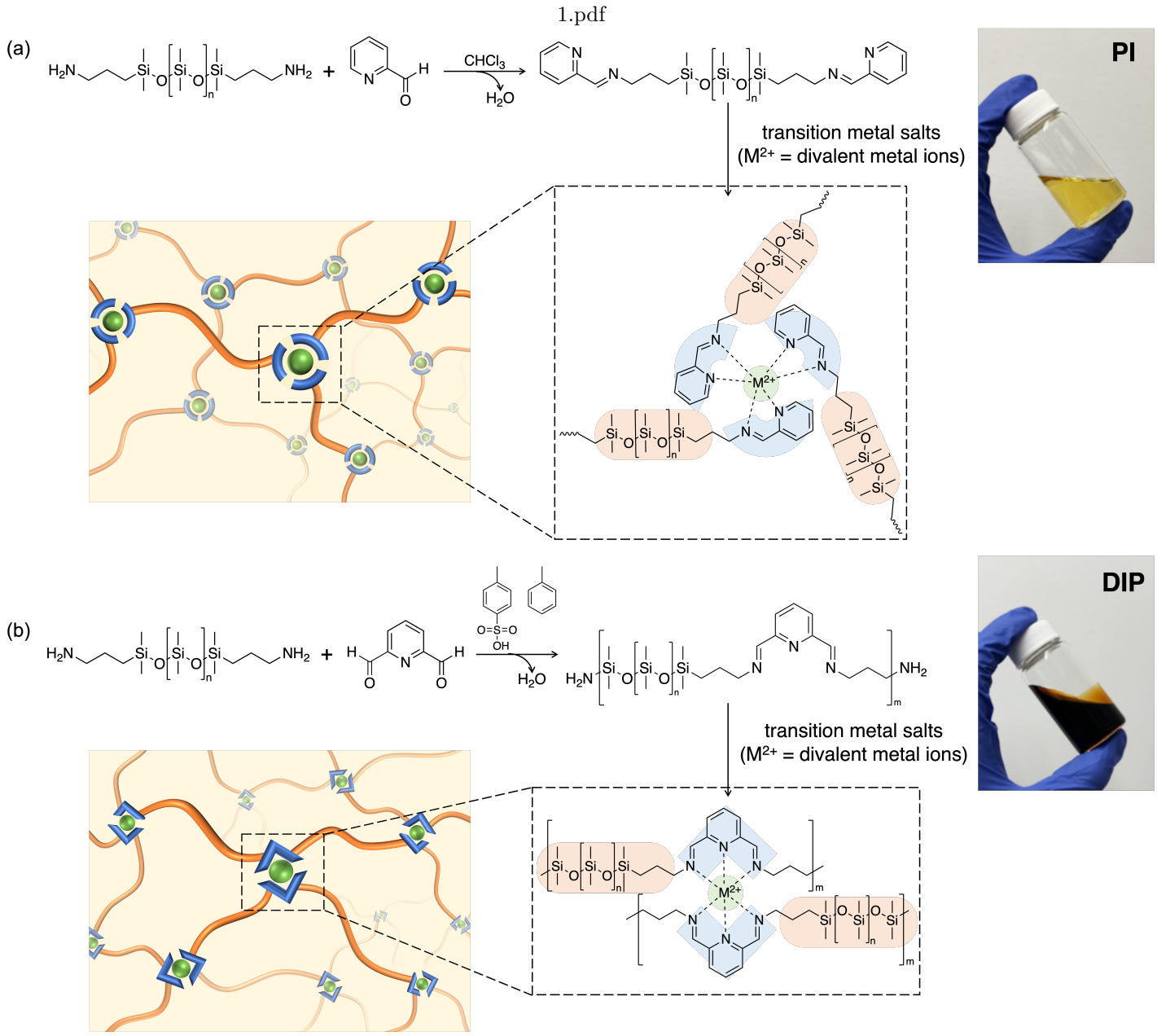

Figure 1: Synthesis of ligand functionalized PDMS and the corresponding metal complexes. (a) The model system: a condensation reaction between aminopropyl terminated PDMS and 2-pyridinecarboxaldehyde was performed to synthesize PI, generating a yellow oil-like liquid. An end-crosslinked network is formed by the coordination of PI with divalent transition metal cations. (b) The control system: a condensation reaction between aminopropyl terminated PDMS and 2,6-pyridinedicarboxaldehyde was performed to synthesize DIP, generating a deep orange colored highly viscous liquid. An inter-crosslinked network is formed by the coordination of the DIP and divalent transition metal cations.

imine functionalized PDMS (named PI) was synthesized through a condensation reaction between the aminopropyl terminated PDMS and 2-pyridinecarboxaldehyde, yielding a yellow colored oil-like liquid (Figure 1a).[42, 45] The structure of PI was verified by ^{1}H-NMR (Figure S1). Gel permeation chromatography (GPC) shows that the number average molecular weight (M_n) of PI is $\sim$ 2000 g/mol (Figure S3), which is far below the critical entanglement value of PDMS ($M_e \sim 10^4$ g/mol).[46] A divalent transition metal salt is added into the PDMS to form a metal-ligand coordinated PDMS network. One metal center is coordinated by three PI chains in an octahedral geometry, forming an end-crosslinked network.[45, 47] To create a clear contrast in PDMS chain dynamics while retaining the metal-ligand coordination density, a control system consisting of diiminopyridine tridentate ligand functionalized PDMS (named DIP) was synthesized through a condensation reaction between aminopropyl terminated PDMS and 2,6-

pyridinedicarboxaldehyde, yielding a deep orange colored highly viscous liquid (Figure 1b).[48] The amine-aldehyde condensation reaction happens at both aldehyde moieties on 2,6-pyridinedicarboxaldehyde. Therefore, the diiminopyridine ligands generated not only provide the coordination ability from the electron-rich nitrogen atoms, but also connect the PDMS precursors into longer chains. The structure of DIP was verified by ^{1}H-NMR (Figure S2). The higher M_n of DIP ($\sim$ 9600 g/mol) compared to PI resulting from the connection of diiminopyridine ligands was confirmed by GPC (Figure S3). When divalent transition metal salt is added, one metal center is coordinated by two diiminopyridine ligands, forming an inter-crosslinked network.[49] The DIP network is expected to be less dynamic than the PI network even when the metal coordination bond dynamics are matched because the DIP chains remain constrained on two ends when a metal coordination bond opens, whereas the PI chains become dangling ends when a metal coordination bond opens.

We chose Zn(II) as the metal cation, because it forms stable octahedral complexes with both pyridyl imine ligands and diiminopyridine ligands.[47, 48] Zinc tetrafluoroborate salt ($Zn(BF_4)_2$) was added into the model system PI and the control system DIP to form fully crosslinked metal-coordinated PDMS networks (named PI-$Zn(BF_4)_2$ and DIP-$Zn(BF_4)_2$, respectively). In both systems, the liquid linear PDMS turns into a solid upon addition of the salt. The coordinated structures were confirmed by Fourier transform infrared (FTIR) spectroscopy (Figure 2a). All the spectra were normalized by the strong absorption band at the wavelength of $\sim$ 1260 cm^{-1}, corresponding to the Si-CH_3 bending vibration on the PDMS backbone.[50] Imine groups have a C=N stretching peak located at $\sim$ 1650 cm^{-1} as free ligands, and the peak shifts to lower wavelength due to the decrease of C=N bond order when forming complexes.[51, 52] Therefore, the height of the C=N stretching peaks at $\sim$ 1650 cm^{-1} decrease after coordination. A new peak arises at $\sim$ 1590 cm^{-1} for PI-$Zn(BF_4)_2$, and similarly, a new peak appears at $\sim$ 1600 cm^{-1} for DIP-$Zn(BF_4)_2$.

To investigate the difference in the dynamic characteristics of the two $Zn(BF_4)_2$-coordinated networks, we performed monotonic and cyclic uniaxial tensile tests (Figure 2b). As shown in the pictures, PI-$Zn(BF_4)_2$ is soft and highly extensible, whereas DIP-$Zn(BF_4)_2$ is stiff and brittle. From the monotonic stress-strain curves, we can see that the network of PI-$Zn(BF_4)_2$ is much weaker than DIP-$Zn(BF_4)_2$, and the difference in Young's modulus (Table S1) is more than 170 times. Furthermore, when increasing the strain, PI-$Zn(BF_4)_2$ shows pronounced softening after yield, implying chains slide past each other easily, resulting in a continuous flow of the material to release the stress.[53] On the contrary, DIP-$Zn(BF_4)_2$ breaks at quite a low strain, $\epsilon \approx 0.2$, without softening, implying the chains are less mobile. The more dynamic behavior of PI-$Zn(BF_4)_2$ compared to DIP-$Zn(BF_4)_2$ can also be seen from the stress response under cyclic loading. PI-$Zn(BF_4)_2$ does not show strain recovery in the unloading process, because the chains flow rapidly to accommodate the deformation, leading to plastic deformation and energy dissipation. The less dynamic DIP-$Zn(BF_4)_2$ unloads primarily elastically, showing significant strain recovery. We expect that the difference in the mechanical properties of the two materials is primarily due to network architecture, but there may also be a contribution of coordination stability resulting from the different ligand species.[54]

We next monitored the surface adaptability of the two $Zn(BF_4)_2$-coordinated PDMS upon water attachment by an optical tensiometer using the sessile drop method.[55, 56, 57] A commercial PDMS (Oomoo® 30) was also measured as a second control. During each measurement, a small droplet of water was deposited on the PDMS coated glass open to the ambient lab environment, and the contact angle variation was monitored by a tensiometer for 20 min. According to the Owens-Wendt, Rabel, and Kaelble (OWRK) method, when applying a liquid on a solid, the solid-liquid interface energy γ_{SL} is

$$\gamma_{SL} = \gamma_S^D + \gamma_S^P + \gamma_L^D + \gamma_L^P - 2\sqrt{\gamma_S^D \gamma_L^D} - 2\sqrt{\gamma_S^P \gamma_L^P} \quad (1)$$

where γ_S^D and γ_S^P refer to the dispersive and polar contributions respectively to the surface energy of a solid, and γ_L^D and γ_L^P refer to the dispersive and polar contributions respectively to the surface energy of a liquid.[58, 59] Combining Equation 1 with Young's equation, we obtain

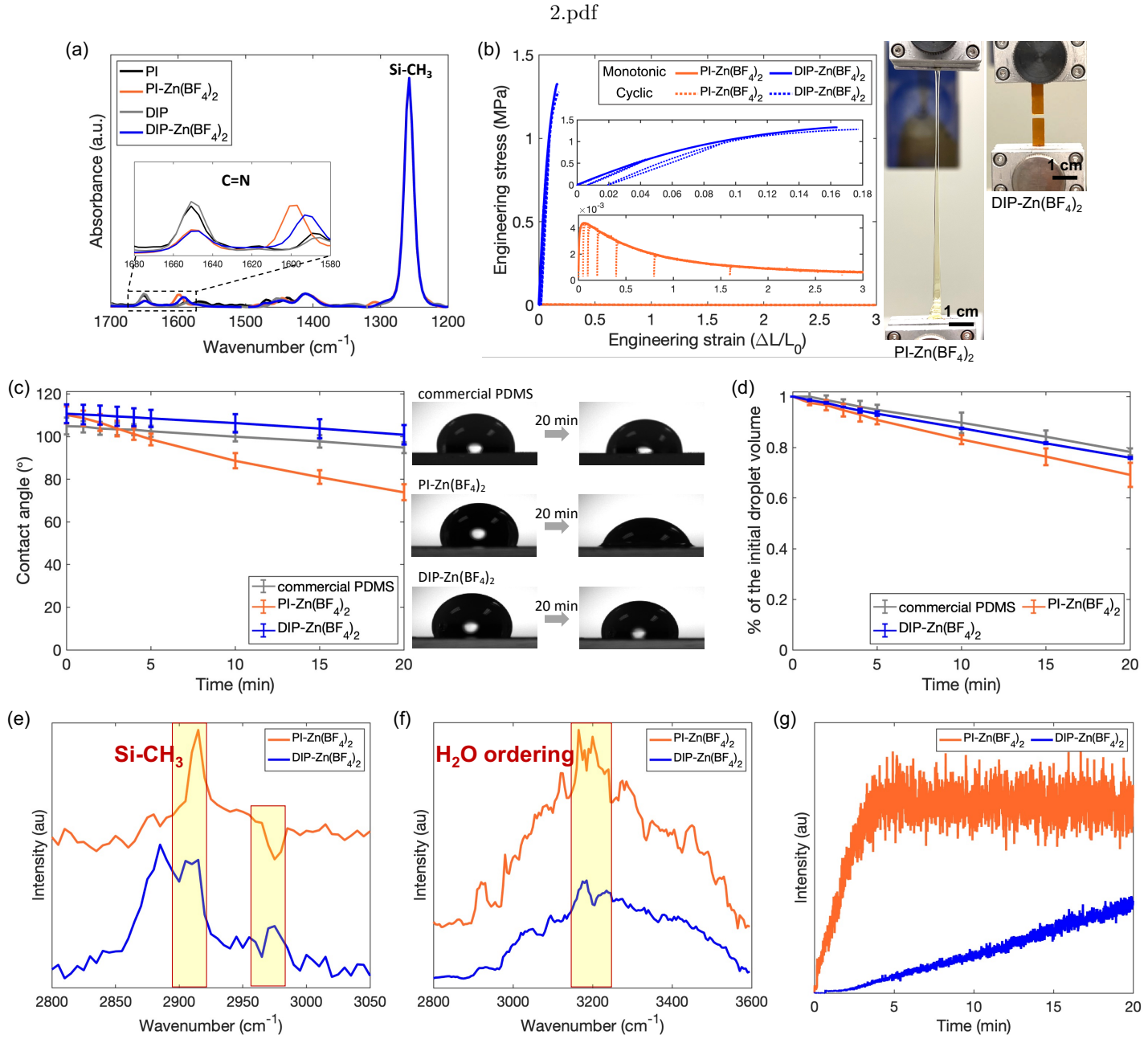

Figure 2: Comparison of $Zn(BF_4)_2$ coordinated PDMS networks. (a) FTIR spectra of PI and DIP before and after $Zn(BF_4)_2$ coordination. (b) Monotonic and cyclic tensile tests plotted as engineering stress as a function of engineering strain and photos of the specimen. Insets are the zoom-in of each material for a better view. (c) Water contact angle evolution on PDMS surfaces and photos of the interface upon droplet application and after 20 *min*. Each data point plotted is the mean value measured from three different spots, and bars show the standard deviation. (d) Change of the droplet volume. Each data point plotted is the mean value measured from three different spots, and bars show the standard deviation. (e) SFG spectra in air. (f) SFG spectra in water after 20 *min*. (g) Time-dependent SFG signal intensity at 3200 cm^{-1}.

$$\cos\theta = \frac{2\sqrt{\gamma_S^D\gamma_L^D} + 2\sqrt{\gamma_S^P\gamma_L^P}}{\gamma_L^D + \gamma_L^P} - 1 \tag{2}$$

where θ is the contact angle at the solid-liquid interface. Equation 2 demonstrates how the water contact angle depends on exposed polar functionalities on a polymer: θ decreases as γ_S^P increases, indicating that the surface is more hydrophilic when the polar contribution increases. In our case, the exposure of polar functionalities governed by network dynamics determines the speed of the transformation towards

hydrophilicity.

The contact angle of the commercial PDMS is $\sim$ 105 ° upon water attachment, and the value drops $\sim$ 10 ° over 20 *min* (Figure 2c, Table S2). As seen in the photos, the contact line between the water droplet and the commercial PDMS surface remains pinned due to the microscopic surface roughness, while the shape of the droplet is flattened.[60] Given that no observable amount of water penetrates into the commercial PDMS substrate, we attribute the decrease of contact angle to water evaporation.[61] For the dynamic system, the contact angle of PI-Zn$(BF_4)_2$ of $\sim$ 110 ° upon water attachment is within the reported range of a typical PDMS surface and indicates the surface is initially hydrophobic.[62] Interestingly, instead of having a pinned contact line, the water droplet slowly spreads out on the PI-Zn$(BF_4)_2$ surface. A dramatic contact angle decrease together with the expanded contact area is observed in contrast to the commercial PDMS. This dynamic wetting behavior results from the dissipation of the excess free energy, which is associated with the increase of interfacial adhesion between the water and the reconfigured polymer, implying the surface has become more hydrophilic.[63] Moreover, as expected, the control system DIP-Zn$(BF_4)_2$ behaves quite similarly to the commercial PDMS. The contact line is pinned and the contact angle drops $\sim$ 10 ° over 20 *min*. This indicates that introducing metal-ligand coordination does not necessarily alter the surface adaptability upon water contact. To better understand the interaction between water droplets and the PI-Zn$(BF_4)_2$ surface, we analyzed the change of droplet volume during the process (Figure 2d, Table S3). A steady decrease is seen for all three materials, with droplets on the PI-Zn$(BF_4)_2$ surface showing faster volume decrease than the two control systems. Referring to the commercial PDMS, for which the droplet volume change simply results from water evaporation, we infer that water adsorption happens on the PI-Zn$(BF_4)_2$ surface, leading to the extra droplet volume decrease. The dynamic nature of the PI-Zn$(BF_4)_2$ network exposes the polar metal-ligand functionality efficiently through rapid chain motion, and thus exhibits faster hydrophilicity progression.[64] The clear contrast between the model system and the control system demonstrates that a properly designed dynamic network that facilities exposing the hydrophilic functionality is crucial.

To test whether this surface adaptation could also be triggered by other polar liquids, we applied ethylene glycol droplets on the PI-Zn$(BF_4)_2$ surface and monitored the change of the droplet over time. A contact angle decrease associated with the contact area expansion can be observed but is less dramatic than the water droplet, due to the relatively lower solvent polarity and no observable evaporation in the initial 20 *min* (Figure S4, S5, Table S5, S6). In contrast, the non-polar silicon oil droplets show a fast and almost perfect wetting on all the PDMS surfaces due to the strong affinity at the solid-liquid interface (Figure S6). To further investigate the reversibility of surface adaptation, we first soaked the PI-Zn$(BF_4)_2$ coated glass slides in water for 2 *hr* (Figure S7). A gently swelled surface is observed, and the contact angle at $\sim$ 67 ° confirms that a hydrophilic surface is developed (Table S7). The samples were then placed under vacuum to completely remove the water. The contact angle on the dried surface was again measured, and found to be consistent with the initial value at $\sim$ 110 °, confirming that a hydrophobic surface is restored.

SFG was used to study the interfacial molecular behavior of PI-Zn$(BF_4)_2$ and DIP-Zn$(BF_4)_2$ to understand the effects of ligands and their associated network architecture on such behavior. SFG spectra collected from the PI-Zn$(BF_4)_2$ and DIP-Zn$(BF_4)_2$ surfaces in air (Figure 2e) are different, showing different surface structures. The PI-Zn$(BF_4)_2$ surface in air is mainly covered by Si-CH_3 groups, as evidenced by the dominating peaks centered at $\sim$ 2910 cm^{-1} and $\sim$ 2960 cm^{-1} (which is negative due to the interference with the non-resonant background) that are contributed by the symmetric and asymmetric C-H stretches of the Si-CH_3 group respectively.[65] Air is a very hydrophobic medium, thus the most hydrophobic Si-CH_3 group in the dynamic PI-Zn$(BF_4)_2$ segregates to cover almost the entire surface with an ordered structure. In contrast, the SFG spectrum collected from the DIP-Zn$(BF_4)_2$ surface in air contains signals from other functional groups (e.g., peak $\sim$ 2885 cm^{-1}), showing the coverage of other functional groups on the surface in addition to the Si-CH_3 groups, because the less dynamic DIP-Zn$(BF_4)_2$ limits the chain arrangement. After exposure to water for 20 *min*, the SFG spectrum changes significantly (Figure 2f and Figure S8). The 3200 cm^{-1} O-H stretching SFG signal is contributed by the strongly hydrogen bonded water molecules at the PDMS/water interface.[66, 67] The PI-Zn$(BF_4)_2$ spec-

trum is strong, showing ordered interfacial water molecules at the interface, due to the now hydrophilic surface of PI-$Zn(BF_4)_2$. The SFG water spectral intensity on the DIP-$Zn(BF_4)_2$ surface is weak, consistent with it remaining hydrophobic. The SFG signal at 3200 cm^{-1} was monitored as a function of time to follow the surface restructuring process after the surfaces were placed in contact with water (Figure 2g and Figure S9). The surface of the more dynamic PI-$Zn(BF_4)_2$ restructures more rapidly than the surface of the less dynamic DIP-$Zn(BF_4)_2$. The SFG time-dependent results are well correlated with the speed of hydrophilic adaptation on the coordinated PDMS surfaces.

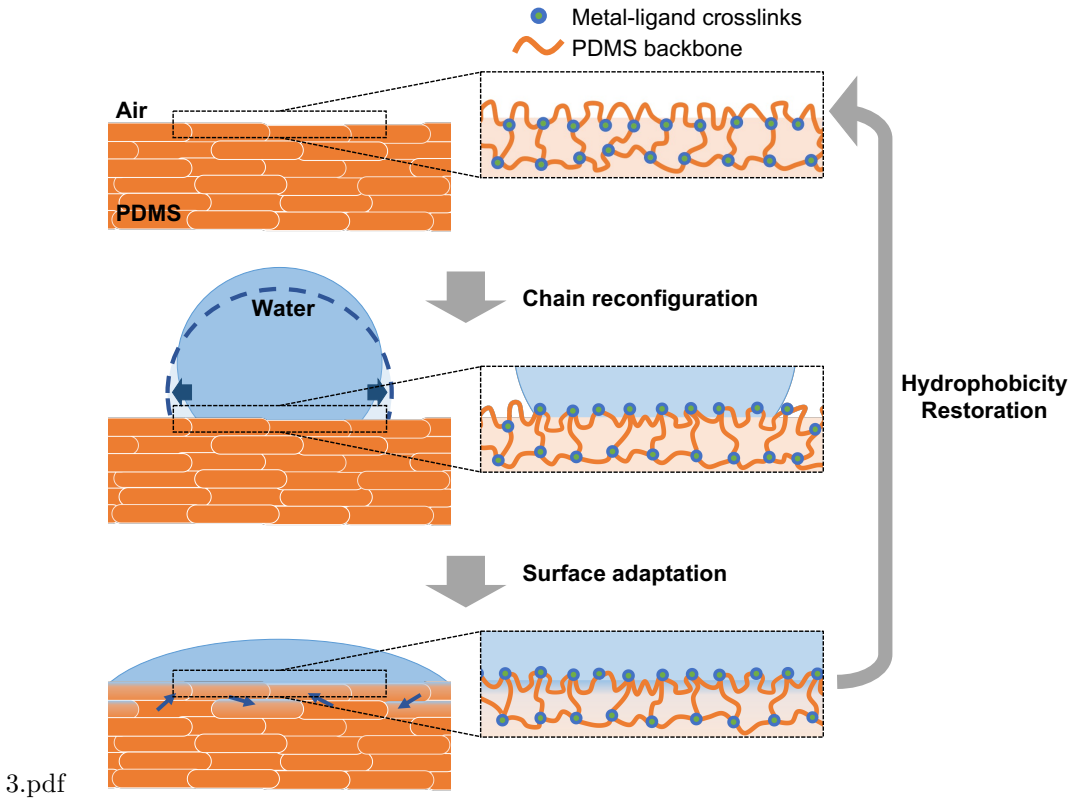

3.pdf

Figure 3: Schematic of the surface adaptation triggered by a water droplet and the surface restoration by removing the water on the metal-ligand coordinated PDMS surface.

Based on what we have learned from the experimental results, the mechanism of the surface adaptation triggered by water interacting with a dynamic metal-ligand coordinated PDMS surface is proposed to explain the hydrophilic progression observed (Figure 3). Prior to the addition of a water droplet, the metal-ligand coordinated PDMS behaves like regular PDMS. The PDMS backbones tend to cover up the surface and the metal-ligand coordination sites lie underneath. This configuration is energetically favorable because the non-polar [$SiO(CH_3)_2$] backbone has lower surface energy than the polar metal-ligand sites.[68] Consequently, the initial contact angles measured for the metal-ligand coordinated PDMS are within the range of the conventional PDMS. When the droplet touches the surface, the hydrophilic metal-ligand coordination sites tend to interact with the water, whereas the hydrophobic PDMS backbone segments tend to repel the water. In a dynamic network, chain reconfiguration can occur. Since the interfacial energy is lowered in the new chain arrangement, the droplet tends to increase the contact area with the surface, so the contact line moves outwards, which triggers chain reconfiguration in the newly wetted area and further lowers the interfacial energy.[69] The wetting process continues, resulting in an elongating contact line and decreasing contact angle. In the meantime, water adsorption happens on the interface due to the strong interaction between the metal-ligand coordination sites and the water molecules. Due to the high mobility, some chains from the bulk migrate to the upper surface gradually and further interact with water. This surface reconstruction process leads to more water adsorption on the surface. On the contrary, if the network is fully constrained or simply less dynamic, chain reconfiguration will be slower, so the wetting resulting from the polarity increase will be too slow to be observed in a relatively

short time period, and instead, evaporation dominates the contact angle change of the droplet.[61] This type of environmentally adaptive surface could have applications in microfluidic devices, where the high intrinsic hydrophobicity and fast hydrophobic recovery of the PDMS microchannels has been a major drawback; and biomimetic actuators, where the locomotion could be powered by the spatial and temporal control of surface wetting.[31, 70]

2.2 Influence of Counter anions

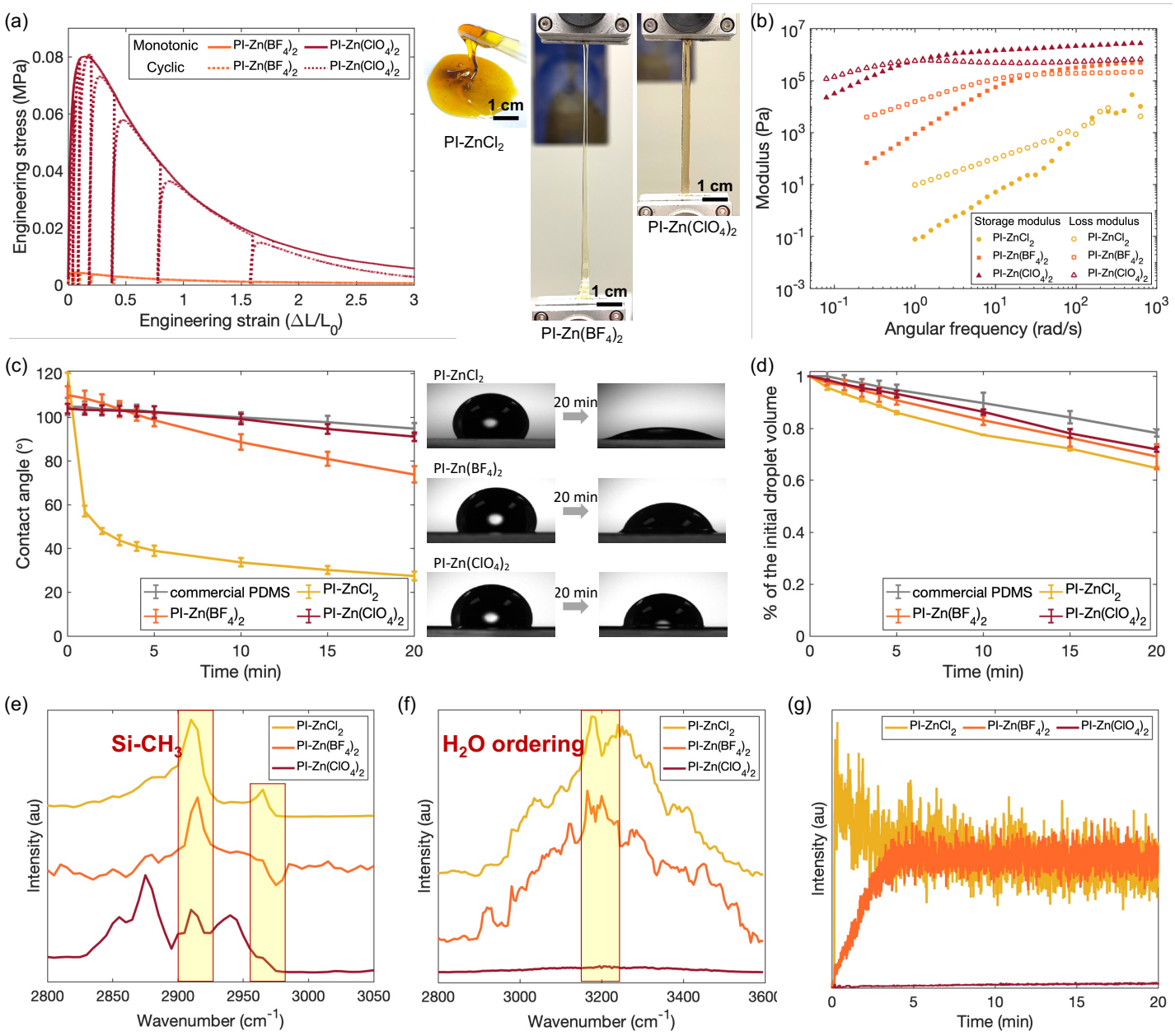

Figure 4: Comparison of the Zn(II)-coordinated PI with different counter anions. (a) Monotonic and cyclic tensile tests plotted in engineering stress as a function of engineering strain and photos of the specimens. (b) Rheological plot of the different materials. (c) Change of the water contact angle on different PDMS surfaces and photos of the interface upon droplet attachment and after 20 *min*. Each data point plotted is the mean value measured from three different spots, and bars show the standard deviation. (d) Change of the droplet volume. Each data point plotted is the mean value measured from three different spots, and bars show the standard deviation. (e) SFG spectra in air. (f) SFG spectra in water after 20 *min*. (g) Time-dependent SFG signal intensity at 3200 cm^{-1}.

Building from our proposed mechanism of the response surface, we next tuned the hydrophilic adaptability of the Zn(II)-pyridyl imine coordinated PDMS by varying the counter anion. Previous studies show that counter anions prompt different strength and kinetics of metal-ligand coordination by interacting with the metal cation, which then further affects the network dynamics.[71, 47] Generally, it is expected that counter anions with larger size and higher charge delocalization will interfere with the metal-ligand coordination less.[72] $ZnCl_2$ and $Zn(ClO_4)_2$ were incorporated into the PI to form Zn(II)-coordinated PDMS (named PI-$ZnCl_2$ and PI-$Zn(ClO_4)_2$, respectively). The formation of these complexes was confirmed by the FTIR (Figure S10). Monotonic and cyclic uniaxial tensile tests were performed on PI-$Zn(ClO_4)_2$ only, since PI-$ZnCl_2$ is too fluid for tensile tests (Figure 4a, Table S8). The stress-strain curve of the monotonic loading shows that PI-$Zn(ClO_4)_2$ goes through a short linear elastic region followed by a long softening regime. The Young's modulus of PI-$Zn(ClO_4)_2$ is about 13 times larger than PI-$Zn(BF_4)_2$. The coordination strength between Zn(II) and pyridyl imine ligand under different counter anions can be identified from the stiffness of the materials: Cl^- generates the weakest coordination and yields the weakest network, BF_4^- is intermediate, and ClO_4^- promotes the strongest coordination and enables the strongest network. Interestingly, although PI-$Zn(ClO_4)_2$ has a much higher elastic modulus than PI-$Zn(BF_4)_2$, still almost no strain recovery is observed for PI-$Zn(ClO_4)_2$ in the unloading process, indicating that the coordination between Zn(II) and pyridyl imine ligand with the presence of ClO_4^- anions is strong yet labile, with the network retaining no memory of its initial configuration. To quantify the coordination lifetime, we performed rheology measurements (Figure 4b, Table S9). Since PI is free from entanglement, the relaxation of the dynamic network is governed by breaking and reforming the reversible crosslinks between Zn(II) cations and the pyridyl imine ligands. The characteristic relaxation time of the material (τ_c), which is equivalent to the coordination lifetime in this case, can be extracted from the reciprocal of angular frequency where the curves of storage modulus and loss modulus crossover each other.[73] As expected, PI-$ZnCl_2$ has the shortest relaxation time, corresponding to a coordination lifetime of $\sim 0.03\ s$. PI-$Zn(BF_4)_2$ has the intermediate relaxation time, corresponding to a coordination lifetime of $\sim 0.24\ s$. PI-$Zn(ClO_4)_2$ has the longest relaxation time, corresponding to a coordination lifetime of $\sim 6.31\ s$.

The hydrophilicity progression of PI-$ZnCl_2$ and PI-$Zn(ClO_4)_2$ was monitored by the optical tensiometer using the sessile drop method. From the wetting behavior of the water droplet on different materials, we see a clear contrast among the three Zn(II)-coordinated PI. The contact angle of the PI-$ZnCl_2$ starts at $\sim$ 120 °, indicating the surface is highly hydrophobic at the beginning, followed by a rapid drop to $\sim$ 40 ° after 5 *min*, and the contact angle keeps decreasing slowly afterwards (Figure 4c, Table S10). This transformation suggests that PI-$ZnCl_2$ has a fast-evolving surface, which exposes the polar functionality rapidly and interacts with water strongly, exhibiting high hydrophilicity. It can be clearly seen from the pictures that the water droplet on the PI-$ZnCl_2$ surface flattens out after 20 *min*. In contrast, the contact angle of PI-$Zn(ClO_4)_2$ starts at $\sim$ 104 ° and decreases $\sim$ 13 ° over 20 *min*, exhibiting the lowest hydrophilicity among the three Zn(II)-coordinated PI. Furthermore, the droplet volume decreases faster on the three Zn(II)-coordinated PI than the commercial PDMS (Figure 4d, Table S11), suggesting that water adsorption happens on the interfaces. The amount of water adsorbed is positively correlated with surface hydrophilicity: a more hydrophilic surface tends to adsorb more water.[64] From the above discussion, we can see that the weaker and more labile metal-ligand coordination enables a more dynamic PDMS network, which exposes the polar functionality more rapidly, and yields a surface with higher adaptability and faster hydrophilic progression.

SFG was used to study the interfacial behavior of PI-$ZnCl_2$ and PI-$Zn(ClO_4)_2$. SFG spectra were collected from the PDMS samples in air and water (Figure 4e, Figure 4f, and Figure S11). These spectra collected in air are different from each other due to the different surface structures of the three PDMS materials in air caused by the varied anions: Cl^-, BF_4^-, and ClO_4^-. The SFG spectrum collected from the PI-$ZnCl_2$ surface in air is dominated by a strong peak centered at around 2910 cm^{-1}, along with a weak peak at around 2960 cm^{-1}, contributed by the symmetric and asymmetric C-H stretching modes of the Si-CH_3 groups, similar to that collected from PI-$Zn(BF_4)_2$ in air. The strong SFG signals indicate that the surface Si-CH_3 groups are very ordered. This shows that the PI-$ZnCl_2$ surface is covered by

the ordered hydrophobic Si-CH_3 groups in air, similar to the PI-$Zn(BF_4)_2$ surface. As discussed above, Cl^- generates the weakest coordination among the three anions and yields the most dynamic PDMS network. SFG spectra collected from the PI-$Zn(ClO_4)_2$ surface in air is different from those detected from PI-$ZnCl_2$ and PI-$Zn(BF_4)_2$. In addition to the peaks contributed by the Si-CH_3 groups, SFG signals (e.g., at 2860 cm^{-1} and 2880 cm^{-1}) are generated from other groups, such as various CH_2 groups including Si-CH_2, C-CH_2, and N-CH_2 groups. Even though air is very hydrophobic, due to the suppressed dynamics of the material, the surface cannot be fully covered by the Si-CH_3 groups. The SFG spectra in water show that the interfacial water molecules have very different interfacial orderings for the surfaces of the three materials. The PI-$ZnCl_2$/water interface generates the strongest SFG water signal with the highest ordering, followed by PI-$Zn(BF_4)_2$ and then PI-$Zn(ClO_4)_2$. As expected, the three surfaces exhibit markedly different time-dependent changes in water (Figure 4g and Figure S12). The SFG signal collected from the PI-$ZnCl_2$/water interface increased immediately after water contact, then decreased over time to $\sim$ 1/2 of the maximum; this overshoot was not observed for any of the less dynamic networks. The overshoot for PI-$ZnCl_2$ is likely due to the strong immediate water interaction as the hydrophilic metal-coordinated moieties move to the surface in response to water contact, followed by a slower adjustment as water is adsorbed into the deeper surface. The time-dependent SFG signal intensity change detected from the PI-$Zn(ClO_4)_2$/water interfaces is the slowest of the three counter anions as expected from the longest crossover time in the rheological measurements, and the smallest contact angle change. The above presented SFG studies on the three PDMS materials in air, in water, and time-dependent surface structural changes in water provide molecular level interpretation on the above contact angle measurement results. Clearly, the different surface adaptation behavior of the three PDMS materials is caused by the different network dynamics as tuned by the choice of counter anion.

2.3 Influence of Metal Cations

5.pdf

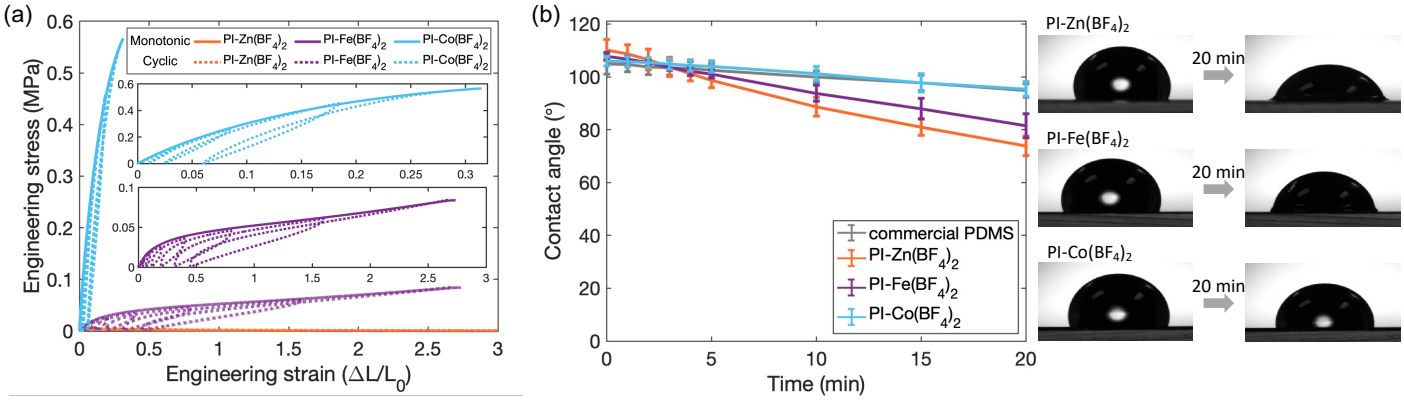

Figure 5: Comparison of different metal cation coordinated PI. (a) Monotonic and cyclic tensile tests plotted in engineering stress as a function of engineering strain. (b) Change of the water contact angle on different PDMS surfaces and photos of the interface upon droplet attachment and after 20 *min*. Each data point plotted is the mean value measured from three different spots, and bars show the standard deviation.

Moving forward, we demonstrate another building block, the metal cation, and its influence on the PDMS hydrophilic adaptability. PI-$Fe(BF_4)_2$ and PI-$Co(BF_4)_2$ were synthesized, and the coordinated structure was confirmed by FTIR (Figure S13). The variation in network dynamics resulting from incorporating different metal cations is characterized by mechanical testing. The stress-strain curves show that the elastic modulus significantly increases from Zn(II) to Fe(II) to Co(II), indicating that the coordination strength has the order of Zn(II) < Fe(II) < Co(II) (Figure 5a, Table S12). Both PI-$Fe(BF_4)_2$ and PI-$Co(BF_4)_2$ show clear strain recovery in the unloading process, but PI-$Fe(BF_4)_2$ recovers less than PI-$Co(BF_4)_2$ and leaves a more pronounced hysteresis, suggesting that the metal-ligand bond kinetics has the order of Zn(II) > Fe(II) > Co(II). Therefore, with the same counter anion, Zn(II) generates the most

dynamic network among the three metal cations, Fe(II) is the intermediate, and Co(II) yields the least dynamic network. Moreover, the difference in hydrophilicity progression of the coordinated PDMS resulting from incorporating different metal cations can be observed from the wetting behavior of water droplets. PI-Fe$(BF_4)_2$ shows faster contact angle decrease than PI-Co$(BF_4)_2$, but still less dramatic than PI-Zn$(BF_4)_2$ (Figure 5b, Table S13). Both PI-Fe$(BF_4)_2$ and PI-Co$(BF_4)_2$ show water adsorption on the surface, but less than PI-Zn$(BF_4)_2$ (Figure S14, Table S14). SFG measurements on the two metal-coordinated PI surfaces again confirm these results (Figure S15, S16 and S17).

To examine the long time hydrophilicity progression on different metal coordinated PDMS surfaces, we placed the PDMS coated glass slides in a chamber to maintain humidity, and measured the contact angle change after 24 hrs (Figure S18). The contact angle of PI-Fe$(BF_4)_2$ drops to $\sim$ 34 ° from the initial value, and the contact angle of PI-Co$(BF_4)_2$ drops to $\sim$ 62 ° from the initial value (Table S15). These results again confirm that the hydrophilicity of the metal-ligand coordinated PDMS network is directly correlated to the network dynamics: among the three metal cations compared, PI-Zn$(BF_4)_2$ yields the most dynamic network, and therefore exhibits the highest surface adaptability and the fastest hydrophilic progression; whereas PI-Co$(BF_4)_2$ yields the least dynamic network, and therefore exhibits the lowest surface adaptability and the slowest hydrophilic progression.

One way to realized short timescale dynamic network behavior and surface adaptation without Zn(II), is by changing to a metal cation that has a tetrahedral coordination geometry with the pyridyl imine ligands, rather than an octahedral one. A tetrahedral coordination geometry will result in a dynamic linear structure, rather than a crosslinked one. We demonstrated this option by investigating the water wetting behavior of the Cu$(BF_4)_2$ coordinated PI. The Cu(II) cations and the pyridyl imine ligands form tetrahedral coordination (Figure S20).[42] A fast hydrophobic to hydrophilic evolution was observed on the PI-Cu$(BF_4)_2$ surface because of the flexibility of the linear chains, followed by a stronger water adsorption (Figure S21, S22, Table S16, S17).

2.4 Application as Marine Antifouling Coatings

One potential application for metal-ligand coordinated PDMS is as a marine fouling-release coating. PDMS is a good candidate for fouling-release coatings due to its low surface energy that promotes weak adhesion of marine organisms. Therefore, the organisms settled on the surface can be easily removed under hydrodynamic shear stresses produced by water during ship movement or water jet cleaning.[74, 75, 76] We used diatoms as a fouling species to examine the fouling release properties of the metal-ligand coordinated PDMS. PI-Co$(BF_4)_2$ was selected as the coating material considering the slow-release hydrophilicity introduced by the Co(II) coordination and the long term stability of the polymer under water. DIP-Co$(BF_4)_2$ and commercial PDMS (Dow Corning® 3-0213) were used as controls. To evaluate the antifouling behavior, standard diatom adhesion and removal assays were carried out (Figure 6a). The density of cells attached to the surface was counted using a Leica LAS X image analysis system attached to a Zeiss Axioscop fluorescence microscope (Figure 6b). Cells viewed under the microscope were observed to move on all the test coatings indicating that acute toxicity was not an issue in this 2-hour assay. Initial attachment densities on the Co(II)-coordinated PDMS coatings and the commercial PDMS coatings were broadly similar (Figure 6c), reflecting similar tendency of cells to attach firmly to the three surfaces. Interestingly, PI-Co$(BF_4)_2$ exhibits a considerably higher removal rate than the controls subject to a hydrodynamic shear stress of 38 Pa in a calibrated water channel.[77] As a result, the density of remaining diatoms is the lowest on the PI-Co$(BF_4)_2$ coatings ($\sim$ 1/3 of the controls) confirming its superior fouling-release properties (Figure 6c). We attribute this to the progressively developed hydrophilicity of PI-Co$(BF_4)_2$ resulting in a strongly bonded hydration layer at the PDMS/water interface, which weakens the attachment of diatoms and facilitates their detachment during hydrodynamic washing. The SFG spectra confirm that the water ordering on the surface of PI-Co$(BF_4)_2$ is much greater than that of DIP-Co$(BF_4)_2$ (Figure S23).

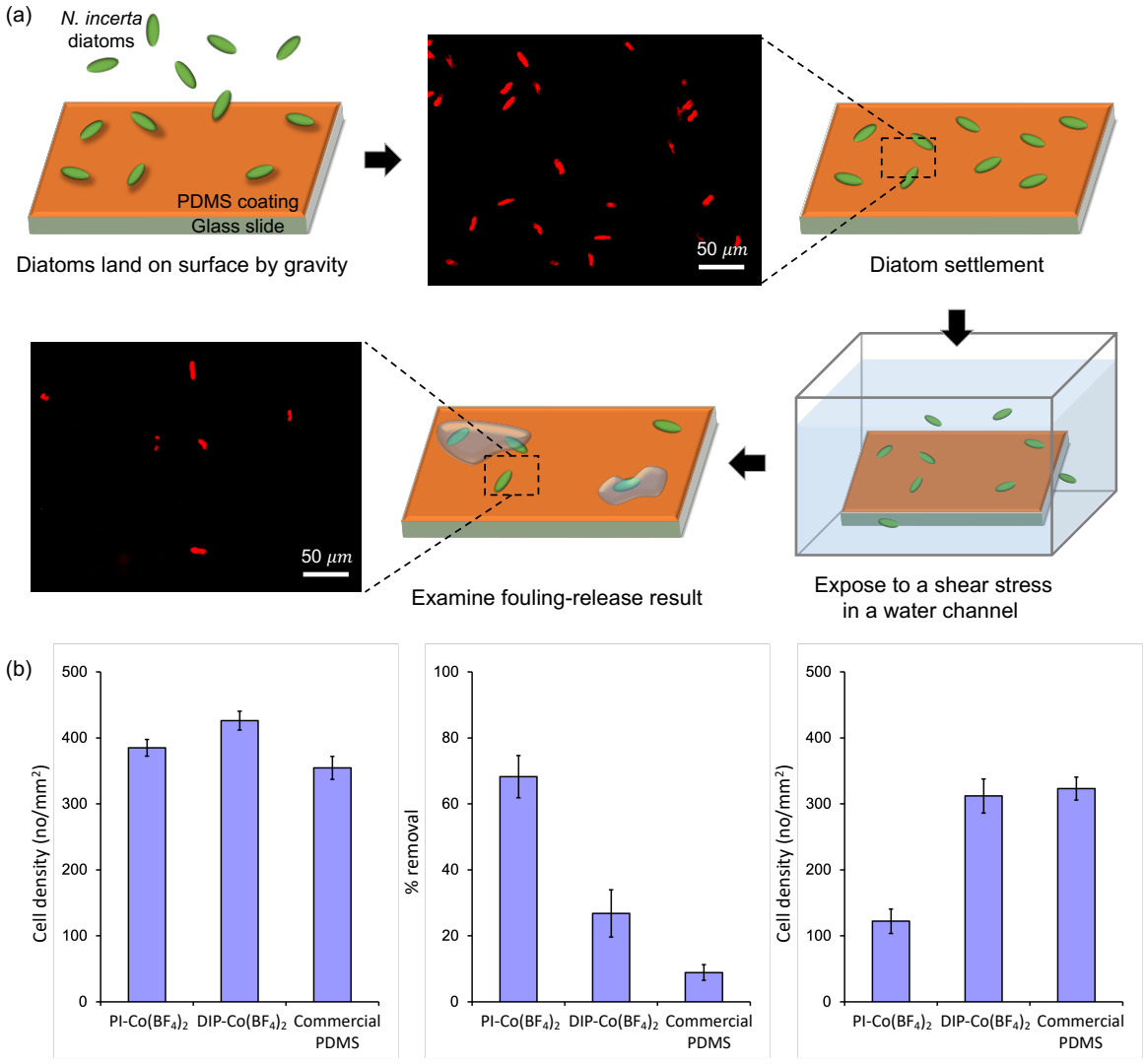

6.pdf

Figure 6: (a) Schematic of the diatom fouling test procedures. Typical diatom cell densities on a PI-$Co(BF_4)_2$ coating before and after exposure to a shear stress are shown next to their respective testing steps. Cells have been fixed and dried and imaged using fluorescence microscopy. (b) Results of PI-$Co(BF_4)_2$ coatings in the diatom fouling test compared to the controls, DIP-$Co(BF_4)_2$ and commercial PDMS. Left: the density of attached diatoms on the coatings after 2 hours. Middle: percent removal of diatoms. Right: the density of diatoms remaining on the coatings after the removal process. Each data point presented is the mean from 90 counts from three replicate slides. Bars show 95% confidence limits.

3 Conclusion

In this manuscript, we introduce and investigate a new method of enabling reversible PDMS surface adaptation with tunable extent and speed by dynamic interactions. Metal-ligand coordination sites embedded in the PDMS matrix introduce polar functional groups which can respond to water exposure, and also set the dynamic characteristics of the network that dominate the progression of hydrophilicity. Moreover, hydrophobicity is restored on the surface once water is removed. We first demonstrated the idea using the pyridyl imine ligand functionalized PDMS, along with the controls consisting of the diiminopyridine ligand functionalized PDMS and commercial PDMS. Both ligand functionalized PDMS were coordinated by the same metal salt ($Zn(BF_4)_2$), and the difference in the network dynamics was carefully investigated by the monotonic and cyclic loading tests: the model system exhibits more dynamic mechanical behavior than the control. The hydrophilicity change of the materials was monitored by water contact angle: the model system exhibits high surface adaptability upon exposure to water, whereas the controls show no change. The interfacial molecular behavior studied by SFG shows that in air, the hydrophobic Si-CH_3 groups in a dynamic PDMS network can segregate to cover almost the entire sur-

face with an ordered structure. When the material is in contact with water, the surface reconstructs and interacts strongly with water molecules at the interface. The results confirm that the material surface adaptability is dominated by the dynamic nature of the network: fast chain motion facilitates the exposure of polar metal-ligand sites, which interact strongly with water, and thus the material exhibits a change in hydrophilicity. Informed by these findings, we manipulated the dynamics of the Zn(II)-pyridyl imine coordinated PDMS by varying the counter anions. The mechanical and rheological characterizations, contact angle results, and SFG studies again confirm that dynamic coordination promotes the exposure of polar functionalities and thus enables strong surface interactions with water. We also show that the dynamic change in hydrophilicity can be tuned by other design factors, such as altering the metal cations in metal-ligand coordination. Lastly, we performed diatom fouling tests on the Co(II)-coordinated PDMS, which shows superior fouling-release properties compared to the controls due to the strongly bonded hydration layer developed at the interface. The insights gained from this work introduce a new concept for developing multifunctional responsive polymer surfaces utilizing dynamic and functional crosslinks, which could be potentially applied in marine antifouling coatings, microfluidic devices, and biomimetic robotics. In future work, this concept will be extended to other polymers and alternative dynamic interactions.

4 Experimental Section

Materials: Aminopropyl terminated polydimethylsiloxane (H_2N-PDMS-N_2H) with the viscosity of $20-30$ *cSt* was purchased from Gelest. 2-pyridinecarboxaldehyde, zinc(II) tetrafluoroborate hydrate, zinc(II) perchlorate hexahydrate, iron(II) tetrafluoroborate hexahydrate, chloroform, toluene, dichloromethane, methanol, tetrahydrofuran, ethylene glycol, and molecular sieves 3A were purchased from MilliporeSigma. 2,6-pyridinedicarboxaldehyde was purchased from TCI Chemical. Zinc(II) chloride hydrate and cobalt(II) tetrafluoroborate hydrate were purchased from Alfa Aesar. Hexane, acetonitrile, and potassium chloride were purchased from Fisher Chemical. P-toluenesulfonic acid monohydrate were purchased from Oakwood Chemical. Toluene and chloroform were dried by activated 3A molecular sieves. All other materials were used as received.

Synthesis of pyridyl imine functionalized PDMS: PI was synthesized via a condensation reaction. The method was from a previously published procedure.[45] H_2N-PDMS-N_2H with the viscosity of $20-30$ *cSt* (50 *g*, 0.03 *mol*) was dissolved in chloroform (100 *ml*), and 2-pyridinecarboxaldehyde (6.6 *g*, 0.06 *mol*) was then added into the solution. 3A molecular sieves (200 *g*) was used to absorb the water generated during the reaction. The mixture was stirred at room temperature for 48 *hr*. Chloroform was then removed under rotary evaporation. The product was redissolved in hexane (50 *ml*) and excess 2-pyridinecarboxaldehyde was extracted by acetonitrile (100 *ml*). The PDMS product was dried by rotary evaporation, and then left in a vacuum oven at 50 °C for 12 *hr* to completely remove the solvent. The final product was filtered through a 0.45 μm PTFE filter, obtaining yellow colored PDMS oil (46 *g*, yield 81%). ^{1}H NMR (500 MHz, $CDCl_3$) δ 8.64 (ddd, $J = 4.9, 1.8, 1.1$ *Hz*, 2H), 8.37 (t, $J = 1.6$ *Hz*, 2H), 7.99 (dt, $J = 7.9, 1.1$ *Hz*, 2H), 7.73 (td, $J = 7.7, 1.9$ *Hz*, 2H), 7.30 (ddd, $J = 7.6, 4.9, 1.4$ *Hz*, 2H), 3.66 (td, $J = 7.0, 1.4$ *Hz*, 2H), $1.82-1.71$ (m, 4H), $0.65-0.50$ (m, 4H), $0.90-0.03$ (m, 155H).

Synthesis of diiminopyridine functionalized PDMS: DIP was synthesized according to a previously reported procedure.[48] H_2N-PDMS-N_2H with the viscosity of $20-30$ *cSt* (50 *g*, 0.03 *mol*) was dissolved in toluene (100 *ml*). 2,6-pyridinedicarboxaldehyde (4 *g*, 0.03 *mol*) and p-toluenesulfonic acid monohydrate (53 *mg*, 0.3 *mmol*) were added into the solution. The mixture was heated to 120 °C in an oil bath and stirred for 10 *hr* under an argon atmosphere. When the reaction finished, the solution was cooled down to room temperature and the toluene was removed by rotary evaporation. The product was then dissolved in dichloromethane (50 *ml*) and transferred into a separatory funnel. Methanol (50 *ml*) was then added to extract the excess 2,6-pyridinedicarboxaldehyde. The mixture was settled to phase separate and the PDMS phase was collected. The product was dried under vacuum to completely remove the solvent, obtaining deep orange colored viscous PDMS oil (35 *g*, yield 65%). ^{1}H NMR (500 MHz,

$CDCl_3$) δ 8.40 (s, 2H), 8.01 (d, $J = 7.3\ Hz$, 2H), 7.78 (t, $J = 7.8\ Hz$, 1H), 3.67 (t, $J = 6.9\ Hz$, 4H), 1.76 (dt, $J = 15.6, 7.9\ Hz$, 4H), $0.65 - 0.56$ (m, 4H), $0.09 - 0.03$ (m, 166H).

Synthesis of metal-coordinated complexes: 2 g ligand functionalized PDMS was dissolved in 20 ml THF, and a certain amount of metal salt calculated from stoichiometry was dissolved in THF (0.1 g/ml) in a separate vial. The metal salt solution was added dropwise into the PDMS solution, and the mixture was stirred until homogeneous. The solution was then concentrated to 5 ml and poured into a Teflon mold or drop cast on a glass slide for the contact angle test. The polymer was dried at ambient atmosphere overnight, and then dried in the vacuum oven at 50 °C for 24 hr.

^1H nuclear magnetic resonance (^1H NMR): The ^{1}H NMR spectrum of the linear polymer was acquired on a Bruker Advance III HD 500 spectrometer. The polymer was dissolved in $CDCl_3$ and processed by 16 scans, with 30 s relaxation delay and 90 ° excitation pulse.

Gel permeation chromatography (GPC): The molecular weight and polydispersity of PI and DIP were conducted on a Waters Ambient Temperature GPC equipped with triple detectors. THF was used as the eluent with a flow rate of 1.00 mL/min. Monodispersed polystyrene was used as standards. The GPC sample was prepared by dissolving the polymer in THF with a concentration of 1 mg/mL and then filtering through a 0.45 μm PTFE filter.

Contact angle tests: All the contact angle measurements were conducted on an Attension Theta Lite tensiometer. Sessile-drop goniometry was used in each measurement. Glass slides coated with polymer were placed horizontally on the platform and a droplet of water or other measuring liquid was placed on the surface. The droplet profile was recorded by the camera for 10 s, and the contact angle at the interface between the substrate and the liquid was analyzed by the software automatically. Each sample was measured multiple times (≥ 3) at different locations, and the contact angle was the statistical average of the measured values.

Mechanical tests: The monotonic and cyclic tensile tests were all carried out on a Zwick-Roell Z010 system with a 20 N capacity load cell. The monotonic tensile tests were performed under a constant engineering strain rate of 0.01 s^{-1}. The cyclic tensile tests were performed under a constant engineering strain rate of 0.01 s^{-1} with the displacement control in the loading direction and the force control with a force of 0.001 N in the unloading direction. Samples were cut into a rectangular shape (L×W×H $\approx$ 40 $mm \times 4\ mm \times 0.8\ mm$), and the initial grip-to-grip separation was set to 20 mm. Each material was measured 3 times.

Rheology tests: The rheology measurements were carried out on a TA Instruments DHR-3 rheometer using the 20 mm-diameter parallel plate. A frequency sweep with 1% oscillatory strain was performed. All the samples were equilibrated at 25 °C for 10 min before start.

Sum Frequency Generation (SFG) vibrational spectroscopy: SFG vibrational spectroscopy is a second order nonlinear optical spectroscopy.[37, 38, 39, 40, 41] SFG theories, equipment, and data analysis have been extensively reported.[37, 38, 39, 40, 41] In an SFG process, two photons of light interact with the same molecule, resulting in the release of a third photon with the combine energy-sum frequency-of the two input photons. Experimentally, a visible pulsed laser (532 nm) and a frequency tunable IR pulsed laser are overlapped spatially and temporally at the interface of interest, resulting in the generation of SFG signals from the interface. Here SFG is a vibrational spectroscopic process, meaning enhanced signals come from IR wavelengths that are in resonance with the vibrational modes of the materials being studied. This generates a vibrational spectrum of the materials. The selection rules of SFG are such that only materials without inversion symmetry can generate SFG signal (under the electric dipole approximation). This means that SFG signals will not be generated from bulk materials, as they are usually centrosymmetric and therefore have inversion symmetry. This means that only the interface between two materials where the inversion symmetry is broken will generate SFG signals. This makes SFG an inherently surface specific spectroscopic technique that allows for the study of interface in situ, nondestructively. This study used a commercial SFG spectrometer from EKSPLA and all the SFG spectra were collected using ssp (s-polarized sum frequency signal, s-polarized input green beam, and p-polarized

IR beam) polarization combinations. [78, 79, 80] In this work, to collect SFG spectra, right-angle CaF_2 prisms (Altos Photonics, Bozeman, MT) were used as substrates. PI and DIP materials used for SFG study were prepared by dissolving 1 g of the appropriate PDMS and the calculated amount of salt based on stoichiometry in separate 5 mL aliquots tetrahydrofuron (THF). Once fully dissolved, the two aliquots of THF were mixed and vortexed at 5000 rpm for 30 min to ensure thorough mixing of the solutions. The materials were then spin coated onto CaF_2 prisms at 2000 rpm for 60 sec. The coated prisms where then dried at 55 ° for 24 hr. Before spin coating, CaF_2 prisms were rinsed with detergent solution, water, ethanol, and toluene. They were then polished and plasma cleaned for 60 sec to ensure no contaminants were on the surface. SFG spectra were collected from the metal PDMS surfaces with variable anion species, metal species, and ligands bound to the PDMS chains using a photomultiplier tube. The SFG spectra of these materials were collected in air in the C-H stretching frequency region of 2800 − 3100 cm^{-1} and in water in the combined C-H/O-H stretching frequency regions, measuring from 2800 − 3600 cm^{-1}. First, the SFG spectrum was collected in air to observe the molecular structure at the PDMS/air interface. Second, the intensity of the SFG signal at 3200 cm^{-1} of the PDMS surface while in contact with deionized water was measured for 20 min to observe interfacial water structural changes over time. Finally, the combined C-H/O-H stretching spectrum was measured with the PDMS material in contact with deionized water after the previous 20 min experiment to observe the surface-water interactions after the system had reached equilibrium. It is worth mentioning that the time-dependent SFG signal intensities were calibrated with the SFG spectra collected in water.

Diatom fouling tests: The metal-ligand coordinated PDMS was coated on glass slides cleaned by piranha solution, with 6 slides for each samples. All coatings were pre-immersed for 48 hr in 0.22 μm filtered artificial seawater prior to the assay in order to equilibrate. Cells of *Navicula incerta* were cultured in F/2 medium contained in 250 ml conical flasks. After 3 days the cells were in log phase growth. Cells were washed 3 times in fresh medium before harvesting and diluted to give a suspension with a chlorophyll content of approximately 0.25 $\mu g/ml$. For initial attachment, cells were settled on three replicate coated slides of each sample in individual quadriPERM® dishes containing 10 ml of suspension at around 20 °C on the laboratory bench. After 2 hr the slides were exposed to 5 min of shaking on an orbital shaker (60 rpm) followed by a submerged wash in seawater to remove cells that had not attached (the immersion process avoided passing the samples through the air-water interface). Samples were fixed in 2.5% glutaraldehyde, air dried and the density of cells attached to the surface was counted on each slide using a Leica LAS X image analysis system attached to a Zeiss Axioscop fluorescence microscope. Cells were visualised by autofluorescence of chlorophyll. Counts were made for 30 fields of view (each 0.15 mm^2) on each slide. For diatom removal, a further three slides of each coating were settled with cells of *N. incerta* as described above. Slides with attached cells were exposed to a shear stress of 42 Pa in a water channel for 5 min.[77] Samples were fixed and the number of cells remaining attached was counted as described above.

Statistical Analysis: The stress-strain curve of a sample presented in the plot is from a single tensile test. The Young's modulus of each sample was calculated from the slope of the linear elastic region of a stress-strain curve, and the value presented in this manuscript is in the format of mean ± standard deviation (SD) by averaging three reproduced tensile tests. All the contact angle results were analyzed by the OneAttension software automatically. Each data point presented in the plot has the format of mean ± SD calculated by averaging at least three reproduced measurements on the surface of one sample at different spots without pre-processing. The SFG signal was normalized using input visible and IR beam intensities. The presentation of the SFG spectra and time-dependent signal change in this manuscript follows the typical way of data presentation in the SFG research community. Each SFG spectrum presented here is the result by averaging at least three reproduced SFG spectra. Each diatom fouling data presented in the plot is the mean from 90 counts from three replicate slides, and the Bars show 95% confidence limits. Matlab and Excel were used for data analysis. No tests of significance were conducted and presented between means of the diatom assays.

Supporting Information

Supporting Information is available from the Wiley Online Library or from the author.

Acknowledgements
The work was supported by the Office of Naval Research under Grants no. N00014-17-1-2989, N00014-20-1-2234, and N00014-20-1-2248 under the administration of PO Dr. Armistead. This work made use of the Cornell Center for Materials Research Shared Facilities which are supported through the NSF MR-SEC program (DMR-1719875).

References

[1] M. Li, A. Pal, A. Aghakhani, A. Pena-Francesch, M. Sitti, *Nature Reviews Materials* **2021**, 1–15.

[2] M. Ilami, H. Bagheri, R. Ahmed, E. O. Skowronek, H. Marvi, *Advanced Materials* **2021**, *33*, 19 2003139.

[3] H. Cui, Q. Zhao, L. Zhang, X. Du, *Advanced Intelligent Systems* **2020**, *2*, 11 2000138.

[4] J. M. McCracken, B. R. Donovan, T. J. White, *Advanced Materials* **2020**, *32*, 20 1906564.

[5] Y.-W. Lim, J. Jin, B.-S. Bae, *Advanced Materials* **2020**, *32*, 35 1907143.

[6] T. J. Jones, E. Jambon-Puillet, J. Marthelot, P.-T. Brun, *Nature* **2021**, *599*, 7884 229.

[7] E. Sachyani Keneth, A. Kamyshny, M. Totaro, L. Beccai, S. Magdassi, *Advanced Materials* **2021**, *33*, 19 2003387.

[8] M. Cianchetti, C. Laschi, A. Menciassi, P. Dario, *Nature Reviews Materials* **2018**, *3*, 6 143.

[9] M. Han, L. Chen, K. Aras, C. Liang, X. Chen, H. Zhao, K. Li, N. R. Faye, B. Sun, J.-H. Kim, et al., *Nature Biomedical Engineering* **2020**, *4*, 10 997.

[10] J. Liu, Y. Gao, Y.-J. Lee, S. Yang, *Trends in Chemistry* **2020**, *2*, 2 107.

[11] Y. Xia, Y. He, F. Zhang, Y. Liu, J. Leng, *Advanced Materials* **2021**, *33*, 6 2000713.

[12] H. Aharoni, Y. Xia, X. Zhang, R. D. Kamien, S. Yang, *Proceedings of the National Academy of Sciences* **2018**, *115*, 28 7206.

[13] Y. Qiao, X. Yin, T. Zhu, H. Li, C. Tang, *Progress in Polymer Science* **2018**, *80* 153.

[14] M. T. Chorsi, E. J. Curry, H. T. Chorsi, R. Das, J. Baroody, P. K. Purohit, H. Ilies, T. D. Nguyen, *Advanced Materials* **2019**, *31*, 1 1802084.

[15] R. J. Wojtecki, M. A. Meador, S. J. Rowan, *Nature Materials* **2011**, *10*, 1 14.

[16] X. Yan, F. Wang, B. Zheng, F. Huang, *Chemical Society Reviews* **2012**, *41*, 18 6042.

[17] P. Chakma, D. Konkolewicz, *Angewandte Chemie* **2019**, *131*, 29 9784.

[18] R. P. Sijbesma, E. Meijer, *Chemical Communications* **2003**, , 1 5.

[19] S. Wang, M. W. Urban, *Nature Reviews Materials* **2020**, *5*, 8 562.

[20] T. Nakano, *Polymer journal* **2010**, *42*, 2 103.

[21] E. Khare, N. Holten-Andersen, M. J. Buehler, *Nature Reviews Materials* **2021**, *6*, 5 421.

[22] D. A. Davis, A. Hamilton, J. Yang, L. D. Cremar, D. Van Gough, S. L. Potisek, M. T. Ong, P. V. Braun, T. J. Martínez, S. R. White, et al., *Nature* **2009**, *459*, 7243 68.

[23] M. Burnworth, L. Tang, J. R. Kumpfer, A. J. Duncan, F. L. Beyer, G. L. Fiore, S. J. Rowan, C. Weder, *Nature* **2011**, *472*, 7343 334.

[24] W. Peng, G. Zhang, Q. Zhao, T. Xie, *Advanced Materials* **2021**, *33*, 34 2102473.

[25] J. Peng, A. P. Tomsia, L. Jiang, B. Z. Tang, Q. Cheng, *Nature Communications* **2021**, *12*, 1 1.

[26] D. Qi, K. Zhang, G. Tian, B. Jiang, Y. Huang, *Advanced Materials* **2021**, *33*, 6 2003155.

[27] M. E. Barry, E. C. Davidson, C. Zhang, A. L. Patterson, B. Yu, A. K. Leonardi, N. Duzen, K. Malaviya, J. L. Clarke, J. A. Finlay, et al., *Macromolecules* **2019**, *52*, 3 1287.

[28] M. P. Wolf, G. B. Salieb-Beugelaar, P. Hunziker, *Progress in Polymer Science* **2018**, *83* 97.

[29] J. O. Bechtold, J. C. Arango, A. Shi, A. Singh, S. A. Claridge, *ACS Applied Nano Materials* **2021**, *4*, 7 7037.

[30] H. Guo, P. Chen, S. Tian, Y. Ma, Q. Li, C. Wen, J. Yang, L. Zhang, *Langmuir* **2020**, *36*, 48 14573.

[31] T. J. Plegue, K. M. Kovach, A. J. Thompson, J. A. Potkay, *Langmuir* **2018**, *34*, 1 492.

[32] L. Li, Z. Yan, M. Jin, X. You, S. Xie, Z. Liu, A. van den Berg, J. C. Eijkel, L. Shui, *ACS Applied Materials & Interfaces* **2019**, *11*, 18 16934.

[33] J. Kang, D. Son, G.-J. N. Wang, Y. Liu, J. Lopez, Y. Kim, J. Y. Oh, T. Katsumata, J. Mun, Y. Lee, et al., *Advanced Materials* **2018**, *30*, 13 1706846.

[34] C. Pan, K. Kumar, J. Li, E. J. Markvicka, P. R. Herman, C. Majidi, *Advanced Materials* **2018**, *30*, 12 1706937.

[35] S. C. Grindy, R. Learsch, D. Mozhdehi, J. Cheng, D. G. Barrett, Z. Guan, P. B. Messersmith, N. Holten-Andersen, *Nature Materials* **2015**, *14*, 12 1210.

[36] N. S. Schauser, G. E. Sanoja, J. M. Bartels, S. K. Jain, J. G. Hu, S. Han, L. M. Walker, M. E. Helgeson, R. Seshadri, R. A. Segalman, *Chemistry of Materials* **2018**, *30*, 16 5759.

[37] Y. Shen, *Nature* **1989**, *337*, 6207 519.

[38] Z. Chen, Y. Shen, G. A. Somorjai, *Annual Review of Physical Chemistry* **2002**, *53*, 1 437.

[39] G. Richmond, *Chemical Reviews* **2002**, *102*, 8 2693.

[40] X. Lu, C. Zhang, N. Ulrich, M. Xiao, Y.-H. Ma, Z. Chen, *Analytical Chemistry* **2017**, *89*, 1 466.

[41] Z. Chen, *Progress in polymer science* **2010**, *35*, 11 1376.

[42] Z. Hu, F. M. Kerton, *Applied Catalysis A: General* **2012**, *413* 332.

[43] J. M. Gichumbi, H. B. Friedrich, B. Omondi, *Journal of Organometallic Chemistry* **2016**, *808* 87.

[44] N. Tsaulwayo, R. T. Kumah, S. O. Ojwach, *Polyhedron* **2021**, *197* 115034.

[45] J. Pignanelli, B. Billet, M. Straeten, M. Prado, K. Schlingman, M. J. Ahamed, S. Rondeau-Gagné, *Soft Matter* **2019**, *15*, 38 7654.

[46] L.-H. Cai, T. E. Kodger, R. E. Guerra, A. F. Pegoraro, M. Rubinstein, D. A. Weitz, *Advanced Materials* **2015**, *27*, 35 5132.

[47] J. Pignanelli, Z. Qian, X. Gu, M. J. Ahamed, S. Rondeau-Gagné, *New Journal of Chemistry* **2020**, *44*, 21 8977.

[48] D.-P. Wang, J.-C. Lai, H.-Y. Lai, S.-R. Mo, K.-Y. Zeng, C.-H. Li, J.-L. Zuo, *Inorganic Chemistry* **2018**, *57*, 6 3232.

[49] P. H. Budzelaar, B. de Bruin, A. W. Gal, K. Wieghardt, J. H. van Lenthe, *Inorganic Chemistry* **2001**, *40*, 18 4649.

[50] L. Wang, Q. Ji, T. Glass, T. Ward, J. McGrath, M. Muggli, G. Burns, U. Sorathia, *Polymer* **2000**, *41*, 13 5083.

[51] Z. Zulu, G. S. Nyamato, T. A. Tshabalala, S. O. Ojwach, *Inorganica Chimica Acta* **2020**, *501* 119270.

[52] T. Chu, L. Belding, A. van der Est, T. Dudding, I. Korobkov, G. I. Nikonov, *Angewandte Chemie International Edition* **2014**, *53*, 10 2711.

[53] Y. Vidavsky, M. R. Buche, Z. M. Sparrow, X. Zhang, S. J. Yang, R. A. DiStasio Jr, M. N. Silberstein, *Macromolecules* **2020**, *53*, 6 2021.

[54] C.-H. Li, J.-L. Zuo, *Advanced Materials* **2020**, *32*, 27 1903762.

[55] D. Bodas, C. Khan-Malek, *Sensors and Actuators B: Chemical* **2007**, *123*, 1 368.

[56] K.-Y. Law, *The Journal of Physical Chemistry Letters* **2014**, *5*, 4 686–688.

[57] J. Drelich, *Surface Innovations* **2013**, *1*, 4 248.

[58] D. K. Owens, R. Wendt, *Journal of Applied Polymer Science* **1969**, *13*, 8 1741.

[59] M. Lejars, A. Margaillan, C. Bressy, *Chemical Reviews* **2012**, *112*, 8 4347.

[60] A.-M. Cazabat, G. Guena, *Soft Matter* **2010**, *6*, 12 2591.

[61] J. K. Park, J. Ryu, B. C. Koo, S. Lee, K. H. Kang, *Soft Matter* **2012**, *8*, 47 11889.

[62] A. Mata, A. J. Fleischman, S. Roy, *Biomedical Microdevices* **2005**, *7*, 4 281.

[63] J.-H. Kim, S. I. Ahn, J. H. Kim, W.-C. Zin, *Langmuir* **2007**, *23*, 11 6163.

[64] H.-J. Wang, X.-K. Xi, A. Kleinhammes, Y. Wu, *Science* **2008**, *322*, 5898 80.

[65] C. Chen, J. Wang, Z. Chen, *Langmuir* **2004**, *20*, 23 10186.

[66] C. Leng, S. Sun, K. Zhang, S. Jiang, Z. Chen, *Acta biomaterialia* **2016**, *40* 6.

[67] C. Leng, X. Han, Q. Shao, Y. Zhu, Y. Li, S. Jiang, Z. Chen, *The Journal of Physical Chemistry C* **2014**, *118*, 29 15840.

[68] M. E. Callow, R. L. Fletcher, *International Biodeterioration & Biodegradation* **1994**, *34*, 3-4 333.

[69] M. Inutsuka, H. Tanoue, N. L. Yamada, K. Ito, H. Yokoyama, *RSC Advances* **2017**, *7*, 28 17202.

[70] H. Zhu, B. Xu, Y. Wang, X. Pan, Z. Qu, Y. Mei, *Science Robotics* **2021**, *6*, 53 eabe7925.

[71] Y.-L. Rao, V. Feig, X. Gu, G.-J. Nathan Wang, Z. Bao, *Journal of Polymer Science Part A: Polymer Chemistry* **2017**, *55*, 18 3110.

[72] R. Díaz-Torres, S. Alvarez, *Dalton Transactions* **2011**, *40*, 40 10742.

[73] X. Zhang, Y. Vidavsky, S. Aharonovich, S. J. Yang, M. R. Buche, C. E. Diesendruck, M. N. Silberstein, *Soft Matter* **2020**, *16*, 37 8591.

[74] A. M. Maan, A. H. Hofman, W. M. de Vos, M. Kamperman, *Advanced Functional Materials* **2020**, *30*, 32 2000936.

[75] A. K. Leonardi, C. K. Ober, *Annual Review of Chemical and Biomolecular Engineering* **2019**, *10* 241.

[76] P. Hu, Q. Xie, C. Ma, G. Zhang, *Langmuir* **2020**, *36*, 9 2170.

[77] M. P. Schultz, J. A. Finlay, M. E. Callow, J. A. Callow, *Biofouling* **2000**, *15*, 4 243.

[78] S. Zhang, J. S. Andre, L. Hsu, A. Toolis, S. L. Esarey, B. Li, Z. Chen, *Macromolecules* **2020**, *53*, 22 10189.

[79] M. Xiao, S. Joglekar, X. Zhang, J. Jasensky, J. Ma, Q. Cui, L. J. Guo, Z. Chen, *Journal of the American Chemical Society* **2017**, *139*, 9 3378.

[80] H. Huang, C. Zhang, R. Crisci, T. Lu, H.-C. Hung, M. S. J. Sajib, P. Sarker, J. Ma, T. Wei, S. Jiang, et al., *Journal of the American Chemical Society* **2021**, *143*, 40 16786.

Table of Contents

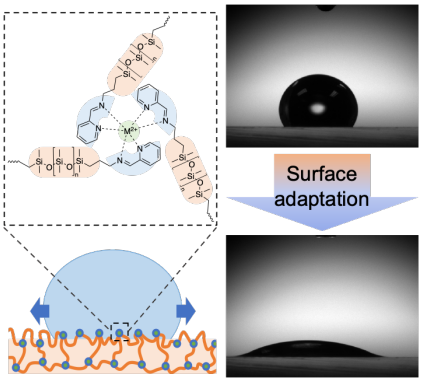

We demonstrated a new design to enable time-dependent adaptation of a polymer via dynamic functionalities. By embedding metal-ligand coordination into a PDMS matrix, a reversible hydrophobic to hydrophilic evolution with tunable extent and speed is realized on the surface when exposed to polar liquids.